Electronic Supplementary Material (ESI) for journal of material chemistry A.

This journal is © The Royal Society of Chemistry 2024

Supporting Information

High yield ammonia production via glucose oxidation assisted electrochemical nitrate reduction

Akansha Chaturvedi,# Sukhjot Kaur,# Kalpana Garg and Tharamani C. Nagaiah*

A Chaturvedi, S. Kaur, K. Garg, T. C. Nagaiah
Department of Chemistry
Indian Institute of Technology Ropar
Rupnagar-140001, India
E-mail: tharamani@iitrpr.ac.in

# Equal contribution

1. Chemical and reagents

All of the chemicals and reagents employed were of analytical quality, and no further purification was done. Cupric chloride (CuCl$_2$ ·2H$_2$O,99 %, extra pure) was purchased from SDFCL, Nickel chloride hydrated (NiC$_{l2}$·6H$_2$O, 98%, extra pure) and thiourea were procured from Loba Chemie. Ammonium chloride (NH$_4$Cl, 99%), potassium nitrate (KNO$_3$, 99%), sodium sulphate (K$_2$SO$_4$, 99%), Salicylic acid (C$_7$H$_6$O$_3$, 99.5%), potassium hydroxide (KOH, 85%), para-dimethylaminobenzaldeyde (p-C$_9$H$_{11}$NO, 99%), sodium nitrate (NaNO$_3$, 99%), sodium nitrite (NaNO$_2$, 98%), sulphanilamide (C$_6$H$_8$N$_2$O$_2$S, 99%), sodium nitroprusside (C$_5$FeN$_6$Na$_2$O, 99%), trisodium citrate (Na$_3$C$_6$H$_5$O7), sodium hypochlorite solution (NaClO, 4-6%), N-(1-Napthyl) ethylenediamine dihydrochloride (C$_{12}$H$_{14}$N$_2$, 99%), hydrazine monohydrate (N$_2$H$_4$.H$_2$O, 99%), were purchased from LOBA chemie. High purity Ar gas (99.999%) was obtained from Sigma. Potassium nitrate (K^{15}NO$_3$ 98 atom% ^{15}N) was obtained from Sigma- Aldrich. Deionised water used in the experiments was obtained from Millipore system (>12 MΩ cm^{-1}).

2. Catalyst synthesis

To synthesize CuNi(1:2)S, initially, CuCl$_2$·2H$_2$O and NiCl$_2$·6H$_2$O were added in 1:2 molar ratio to 1:1 ratio of water and ethylene glycol mixture and stirred to obtained a homogeneous mixture. Afterwards thiourea (CH$_4$N$_2$S) was added to the above solution under constant stirring. The prepared precursor was immediately transferred to a Teflon hydrothermal reactor and heated for 24 h at 200 °C. The resulting black solid was obtained and extensively rinsed with a solution containing ethanol and deionized water, and subsequently dried at 80°C for 6-8 h. Various combinations of binary metal sulphides were synthesized by altering the ratio of Cu to Ni ((1:1) and (1:2)). To prepare only NiS, the copper source was omitted, and in the same way, to create Cu$_x$S, Ni salt was not included, while keeping all other synthesis conditions unchanged.

3. Instruments and characterization

Powder X-ray diffraction (PXRD)

The structural attributes of the obtained catalysts were analyzed using powder X-ray diffraction (P-XRD), and the pattern was recorded using PANalytical X'Pert Pro diffractometer in the 2θ range of 10-60° with a scan speed of 2° per minutes using Cu-Kα radiation (λ = 0.1542 nm, 40 kV, 40 mA).

Scanning electron microscopy

The morphologies of microstructure of all the catalysts were evaluated by field emission scanning electron microscopy (FE-SEM) (ZEISS Ultraplus-4095). For evaluating the elemental distribution energy dispersive X-ray spectroscopic technique (EDS; Oxford INCAx-act, 51-ADD0013) was utilized.

X-ray photoelectron spectroscopy (XPS)

The chemical state distribution of the elements were analyzed by XPS with Thermo scientific NEXSA surface analysis with a micro- focused (400 μm, 72 W, 12000 V) monochromatic Al Kα (1486.6 eV) hemispherical analyzer and 128 channel plate detector under ultrahigh vacuum (UHV 8-10 mbar). The work function of the catalyst were calculated using Ultraviolet photoelectron spectroscopy (UPS) measurements on a Thermo Fisher Scientific Escalab. For UPS, helium gas was used in the gas discharge lamp, and the HeI (21.22 eV) emission line was employed.

UV-Vis spectrophotometry

UV-Vis measurements were obtained using Shimadzu UV-2600 spectrometer.

In-situ electrochemical Raman spectroscopy

In-situ Raman spectroscopic measurements were conducted using a LabRAM HR800 confocal microscope equipped with a 532nm laser excitation source integrated with Autolab 302-N potentiostat/galvanostat controlled by NOVA 1.11 software. LabSpec6 software was used for data acquisition. The data was recorded by using a 50× objective lens (numerical aperture = 0.5) with acquisition time of 30 s and accumulation time of 10 s.

[1]H-Nuclear magnetic resonance (NMR) spectroscopy

NMR spectra were analysed using a JEOL JNM-ECS 400 Hz spectrometer at ambient probe temperatures and referenced as follows: [1]H: residual internal $CHCl_3$ 7.26 ppm; DMSO-d_6 2.50 ppm by using water suppression.

Work function calculation from UPS spectra:

The work function (WF) was calculated using the equation:

$$WF = h\nu - |E_{cutoff} - E_f|$$

where $h\nu$ (21.22 eV) is the photon energy of the excitation light and E_f is the Fermi level determined by fitting a straight line into the leading edge.[1, 2]

4. Electrochemical measurements and analysis

Electrochemical measurements for nitrate reduction reaction

All electrochemical investigations were conducted in a two-compartment H-type cell with a Nafion N-117 membrane separating the two compartments. In order to preserve the proton conductivity of the Nafion membrane, it was cleaned regularly. Firstly, it was boiled for 30 minutes in deionized water, followed by boiling for 1 hour in H_2O_2. The membrane was then boiled for 2 hours in a solution of 0.5 M H_2SO_4 and rinsed multiple times with deionized water. All electrochemical investigations were conducted using a conventional three-electrode assembly with a catalyst-coated nickel foam (0.5 x 0.5 cm^2) as the working electrode (WE), Hg/HgO/1 M NaOH as the reference electrode, and a graphite rod as the counter electrode. Prior to electrochemical investigations, nickel foam was initially treated with a 3 M HCl acid solution, followed by ethanol and distilled water. The catalyst slurry was prepared by physically grinded 1.25 mg of catalyst with a mortar and pestle, then dispersing the catalyst in 20 µL IPA and 480 µL of deionized water for 30 minutes to form a homogenous slurry. For the preparation of the working electrode, 100 µL (0.25 mg) of prepared slurry was drop-casted onto the Ni foam and was then air-dried. The electrochemical measurements were conducted using a Biologic VSP-300 potentiostat equipped with a FRA7M module and EC Lab V11.12 software. Initially, Linear sweep voltammetry (LSV) was performed at a scan rate of 25 mV s^{-1} in an Ar saturated 1 M KOH with and without KNO_3. The true onset potential for NO_3RR was determined without magnetic stirring the electrolyte solution. After that chronoamperometry was performed at various potentials for one hour with continuous magnetic agitation at 500 rpm the electrolyte solution was collected from the cathodic chamber to quantify the products formed. For uniformity, the potentials are converted to RHE, as shown in the following equation (1):

$$E_{RHE} = E°_{Ag/AgCl} + E_{Ag/AgCl} +0.059 \text{ pH} \qquad (1)$$

Here, alkaline medium was used for NO_3RR because it is thought to have a decreased probability of producing hazardous intermediates in solution (such as, NH_2OH and nitrogen oxides), as opposed to those in acidic or neutral media and the need to remove NO_3 ions present in alkaline nuclear wastewater stream.[3-5] Furthermore, in order to ensure that the ammonia generated is much greater than that from environmental pollutants, we fixed the quantity of NO_3^- concentration to 100 mM KNO_3.

Electrochemical measurements for glucose oxidation reaction

All the GOR measurements were carried out using an Autolab 302-N potentiostat/galvanostat managed by NOVA 1.11 software and a Biologic (VSP 300) potentiostat/galvanostat with FRA7M module controlled by EC-Lab V11.12 software. 1 M KOH and 1 M KOH + 100 mM glucose were used for the analysis, which included LSV, and chronoamperometry. The electrochemical characterizations were performed at a fixed scan rate of 5 mV s^{-1}.

Electrochemical measurements for full cell NH$_3$ production

A two compartment H-cell arrangement separated by a Nafion membrane was employed to carry out the NH$_3$ production under full-cell conditions. First, the experiment was carried out using 1 M KOH + 100 mM KNO$_3$ on the cathode side and 1 M KOH on the anode side of the H-cell with CuNi(1:2)S as anode and cathode catalyst over Ni foam to produce NH$_3$ at the cathode and O$_2$ at the anode. Second, to replace OER with GOR at the anode, the anodic solution was changed with 100 mM glucose + 1 M KOH electrolyte. After 1 h of electrolysis in each cell, the amount of NH$_3$ generated was measured.

Quantification of ammonia

(1) Indophenol blue method[6]

The NH$_3$ synthesised was detected by indophenol blue method. 2 ml of diluted sample or standard solution was mixed with 2 ml of colouring solution (1 M KOH solution comprising of 5% TSC and 5% salicylic acid), 1 ml of oxidising solution (0.05 M NaClO) and 0.2 ml of catalyst solution (1% Na$_2$(NO)(CN)$_5$.2H$_2$O). UV-Vis spectrophotometric measurements were measured after 2 h of staining the sample with indophenol indicator. At a wavelength of 655 nm, the calibration curve revealed an good linear relationship between absorbance and NH$_4$Cl concentration.

(2) Nessler's reagent method[6]

Nessler's reagent test verified the NH$_3$ yield determined using the Indophenol blue procedure. Nessler's reagent was made by dissolving 2.5 g of mercuric iodide in 5 mL of potassium iodide aqueous solution and diluting it to 20 mL with deionized water. Then, 4 g of NaOH was added to the above solution and termed as Nessler's reagent. After electrolysis, in 5 mL of diluted electrolyte, and 0.25 mL of 500 g/L sodium potassium tartrate and 0.25 mL of Nessler's reagent were added. After resting for 10 minutes, the UV-Vis spectra of the aforementioned solution was measured, with absorption estimated at 420 nm. The calibration curve was created using a known quantity of NH$_4$Cl and demonstrated a linear connection between absorbance and concentration.

(3) Isotope labelling experiments

The isotope labelling experiment was performed using K^{15}NO$_3$ (Sigma-Aldrich 98 atom% ^{15}N) as the feeding gas to confirm the genuine source of generated NH$_3$ during NRR. The 50 mM K^{15}NO3 was added to 1 M KOH and solution was saturated by Ar gas which was first passed through alkaline KMnO$_4$ followed by H$_2$SO$_4$ solution before passing to set-up cell, electrolysis was conducted -0.4 V vs. RHE for 1 h (Fig. 5c). After electrolysis 500 µL of the electrolyte solution was diluted and 1 mL of diluted electrolyte was taken and mixed with 1 M HCl. The ammonia produced was quantified by using ^{1}H nuclear magnetic resonance (^{1}H NMR) measurements with water suppression method.

A single pulse sequence with 8000 transient scans and an acquisition duration of 2.18 s was used during the relaxation latency of 1 s. 0.7 mL of the above electrolyte solution was obtained, and 0.2 mL of DMSO-d6 was added as an internal standard to get an adequate lock signal, and 0.125 mL of maleic acid was further added for quantification. Other samples ($K^{14}NO3$ and without KNO_3) were evaluated in the same way. With a total of 1024 scans, calibration curves were measured for varied concentrations of standard $^{14}NH_4Cl$ and $^{15}NH_4Cl$ solutions ranging from 1 to 3 ppm with reference to maleic acid as a standard.

Measurement of NH₃ yield rate and Faradaic efficiency (F.E.)

NH₃ yield and F.E. were measured by following equation:

$$NH_3 \; yield = \frac{C \times V}{A \times t}$$

$$FE \; (NH_3) = \frac{8 \times C \times V \times F}{Q}$$

$$NO_2^- \; yield = \frac{C \times V}{A \times t}$$

$$FE \; (NO_2^-) = \frac{2 \times C \times V \times F}{Q}$$

Where C is concentration of product, V is volume of electrolyte, A is area of electrode (cm²), t is electrolysis time, F is faraday constant (96485 C/mol) and Q is total charge passed during electrolysis.

Determination of hydrazine (N₂H₄)

Watt and Chrisp method[7] was used for N_2H_4 detection. The calibration curves were measured for various concentrations of $N_2H_4.H_2O$ solution ranging from 0.0 ppm to 1.0 ppm. 3 ml of the sample or standard solution was combined with 3 ml of the colouring agent (5.99 g p-$C_9H_{11}NO$, 30 ml HCl, and 300 ml C_2H_5OH). After resting for 10 minutes, the UV-Vis spectra of the aforementioned solution was measured in the 600-400 nm region. The resultant plot demonstrates a good linear relationship between absorbance and N_2H_4 concentration.

Determination of Nitrite (NO₂⁻)[8]

Griess method[9] was used to determine the concentration of nitrite using a UV-Vis spectrophotometer at 540 nm. $NaNO_2$ standard solutions with concentrations ranging from 0 to 2.5 ppm were prepared. 0.5 g of sulfanilamide was dissolved in 50 mL of 2 M HCl solution to make the colouring reagent 1. To make reagent 2, 20 mg of N-(1-Naphthyl) ethylenediamine dihydrochloride was dissolved in 20 mL of water. 100 µL of reagent 1 was added to the 5 mL standard or diluted sample solution, and after approximately 10 minutes of resting, 100 µL of reagent 2 was added to the aforesaid solution After resting the solution for 30 minutes, UV-Vis measurements were taken in the range of 450 to 650 nm. The obtained concentration-absorbance standard curves, showing a linear relationship.

Detection of hydroxylamine (NH₂OH)[10]

The amount of NH_2OH was determined by its ability to convert ferric ion (Fe^{3+}) to ferric ion (Fe^{2+}), which, when combined with 1,10-phenanthroline, creates an orange complex. In particular, 100 µL of an aqueous acetate buffer (1 M sodium acetate and 1 M acetic acid combination), 100 µL of a 4 mM ammonium ferric sulphate aqueous solution, and 100 µL of a 10 mM 1,10-phenanthroline ethanolic solution were added successively to 3mL of the sample. The resultant solutions were assessed using UV-Vis absorption spectra based on their maximum absorbance at 510 nm, and the concentration was

quantified using a calibration curve created using a series of standard samples with known hydroxylamine concentrations.

Electrochemical surface area (ECSA) analysis

Electrochemical active surface area was measured by performing CV in non-faradaic region from 0.0 V to 0.1 V *vs*. RHE at various scan rate of 20 to 200 mV s^{-1}. Capacitance double layer (C_{dl}) was determined by the slope of average current density ($(Ia+Ic)/2$) *vs*. scan rate. The ECSA was determined by dividing C_{dl} with specific capacitance of the flat standard surface (20-60 μF cm^{-2}). For our present study we considered it to be 40 μF cm^{-2}.

ECSA = C_{dl}/C_s

where C_s is specific capacitance

Turn over frequency (TOF) for CuNi(1:2)S catalyst calculation:

$$Turn\ over\ number\ (TON) = \frac{NH_3\ yield\ (mg)}{Catalyst\ loading\ (mg)}$$

$$TOF = \frac{TON}{Time\ (h)}$$

Where, NH$_3$ yield is determined by quantifying NH$_3$ after electrolysis at -0.4 V *vs*. RHE and Time is the time of electrolysis in hours.

Hence, TON and TOF for CuNi(1:2)S catalyst is calculated as follows:

$$TON = \frac{1.192}{0.1} = 11.92$$

$$TOF = \frac{11.92}{1} = 11.92$$

$$TOF = 11.92\ h^{-1}$$

Energy efficiency for CuNi(1:2)S calculation:

The NH$_3$ energy efficiency for CuNi(1:2)S catalyst was calculated by the following equation[11, 12]

$$Energy\ efficiency = \frac{\left(1.23 - E^0_{NH_3}\right)F.E._{NH_3}}{1.23 - E}$$

$$Energy\ efficiency = \frac{(1.23 - 0.69)93.44}{1.23 - (-0.4)}$$

$$Energy\ efficiency = 30.95\ \%$$

Where, $E^0_{NH_3}$: equilibrium potential of NO$_3$RR to NH$_3$, which is 0.69 V.

$F.E._{NH_3}$: Faradaic efficiency for NH$_3$

Equilibrium potential of water oxidation: 1.23 V

E: applied potential *vs.* RHE

Extraction of pure ammonia synthesis:

To obtain pure NH$_3$(aq) product, 50 mL of electrolyte solution after electrolysis for 50 h at 100 mAcm^{-2} current density was subjected to distillation process (Scheme S1). The condensed NH$_3$(aq) product was analysed by ^{1}H NMR and quantified by UV-Vis spectroscopic measurement. The condensation efficiency of the NH$_3$ (aq) product was calculated by:

$$Condensation\ collection\ efficiency\ of\ NH_3\ (aq) = \frac{Conc.\ of\ collected\ NH_3\ (aq)}{Conc.\ of\ intial\ NH_3} \times 100$$

Further, the condensed NH$_3$(aq) was treated with 0.4 M HCl to obtained NH$_4$Cl and then after dried by rotary evaporator, and collected powder was further dried at 75°C in oven overnight. The obtained NH$_4$Cl(s) was measured by weighing balance, and analysed by XRD analysis. The collected efficiency of obtained solid NH$_4$Cl powder was calculated as:

$$Collection\ efficiency\ of\ NH_4Cl\ (s) = \frac{Collected\ dried\ NH_3\ in\ NH_4Cl\ (s)}{condensed\ NH_3} \times 100$$
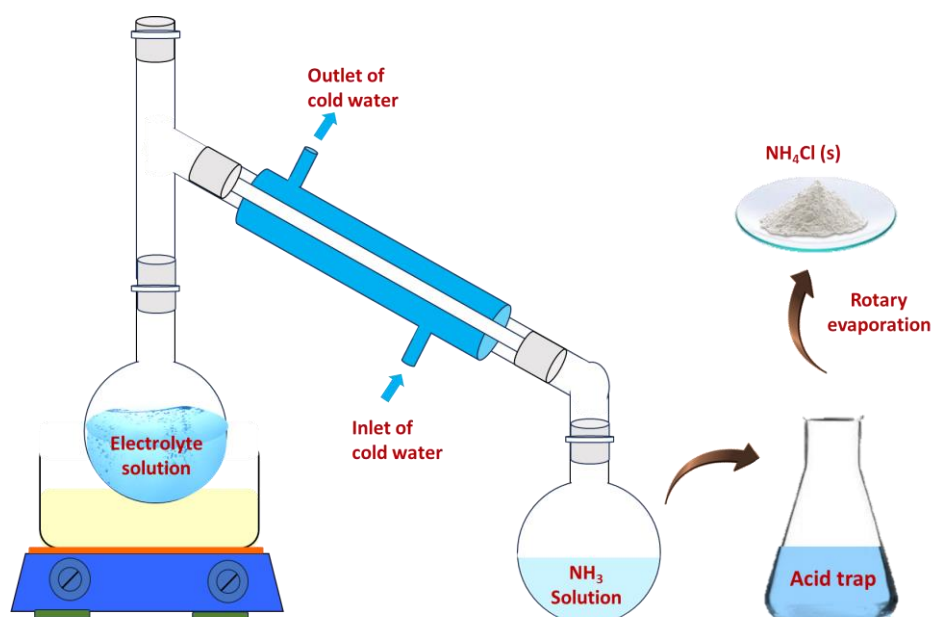
Scheme S1. Schematic representation of extraction of NH$_3$ (aq) product and solid NH$_4$Cl after electrochemical nitrate reduction by distillation.
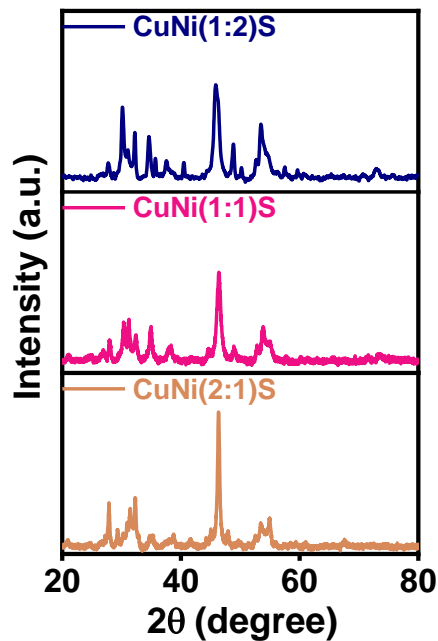
Fig. S1. Comparison of the P-XRD spectra for CuNi(1:1)S, CuNi(2:1)S and CuNi(1:2)S catalyst.
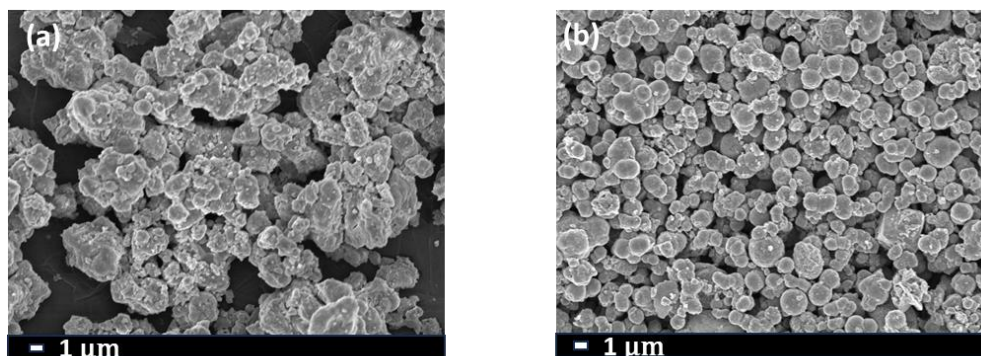
Fig. S2. FE-SEM image for (a) NiS, and (b) Cu_xS catalyst.

Table S1: Comparison table for work function calculated from UPS from Fig. 2e.

Catalyst	E_{cutoff} (eV)	E_{fermi} (eV)	Work function (eV)
NiS	17.94	2.52	5.8
CuS	16.8	2.17	6.59
CuNi(1:2)S	17.11	2.22	6.33
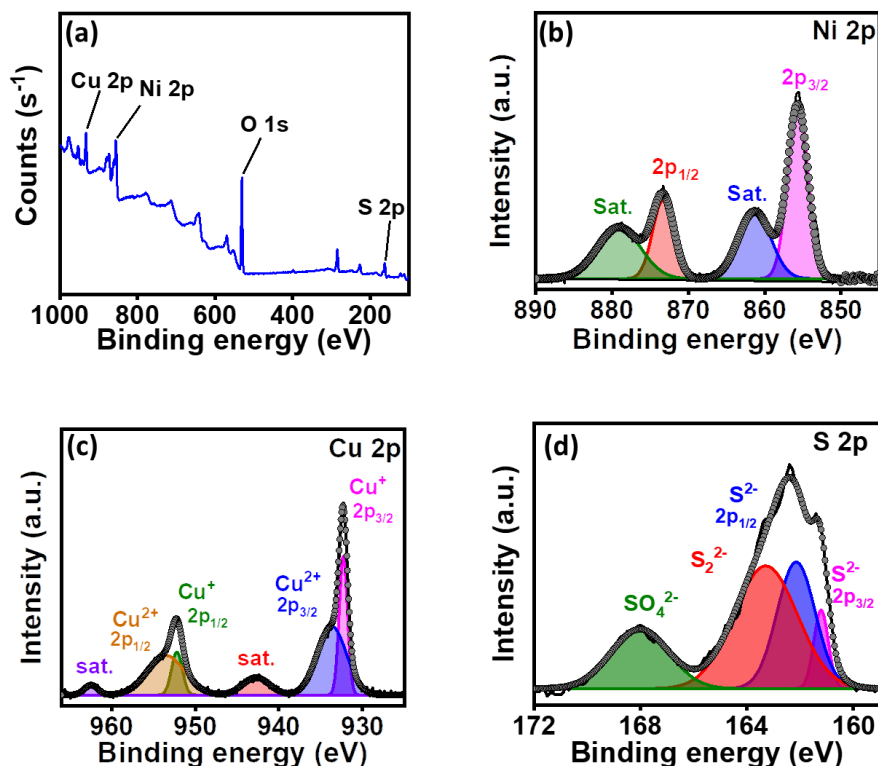
Fig. S3. (a) XPS survey spectra and deconvoluted XP spectra of (b) Ni 2p, (c) Cu 2p and (d) S 2p for CuNi(1:2)S catalyst.

Effect of nitrate concentration studies

The effect of nitrate concentration on the electrochemical nitrate reduction performance was examined. As depicted in Figure S4A, the Faradaic Efficiency (F.E.) increases with higher NO_3^- concentrations, reaching its peak at 100 mM NO_3^-. However, further increasing the NO3- concentration to 1M causes the F.E. to decline. Interestingly, the F.E. for ammonia production also diminishes at 1M NO_3^-. This reduction might be attributed to the high concentration of ammonia produced, which may not be promptly removed from the catalyst surface, leading to the deactivation of the active sites for nitrate reduction.[13]
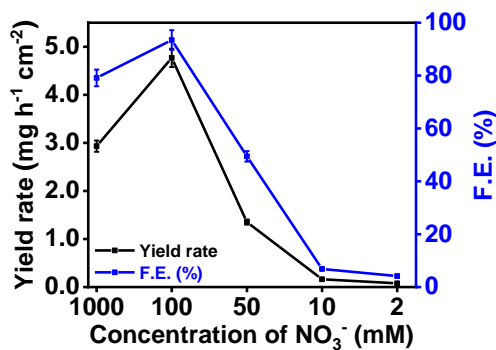
Fig. S4A: NH$_3$ yield rate and F.E. of NO$_3$RR on CuNi(1:2)S catalyst in 1 M KOH solution with various concentration of (2, 10, 50, 100, 1000 mM) KNO$_3$.
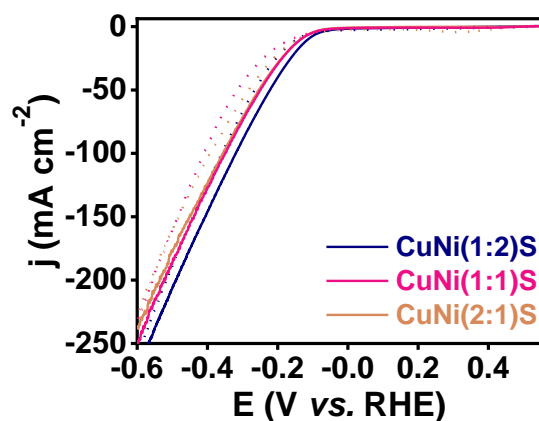
Fig. S4B. LSV of CuNi(1:1)S, and CuNi(2:1)S and CuNi(1:2)S catalyst in Ar saturated 1 M KOH solution in the presence (solid line) and absence of 100 mM KNO_3 (dashed line).

Table S2: Onset potential and net current density at -0.6 V *vs*. RHE derived from LSV (Fig. 3a and S4).

Catalyst	E onset (V)	j (mA cm^{-2}) at -0.6 V *vs*. RHE
NiS	-0.25	155
CuS	-0.22	194
CuNi(1:2)S	-0.095	270
CuNi(1:1)S	-0.14	248
CuNi(2:1)S	-0.14	237

Table S3: Comparison table for TOF calculated from NH_3 yield obtained after electrolysis

for 1 h at -0.4 V *vs*. RHE.

Catalyst	Turn over frequency (h^{-1})
NiS	2.03
CuS	5.0
CuNi(1:2)S	11.92
CuNi(1:1)S	7.8
CuNi(2:1)S	8.4
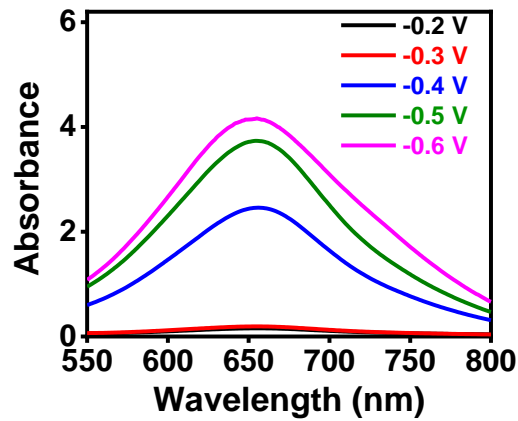
Fig. S5. UV-Vis spectrum obtained by the Indophenol blue method for CuNi(1:2)S with 4 times dilution of electrolyte after chronoamperometric for 1 h at different potentials.
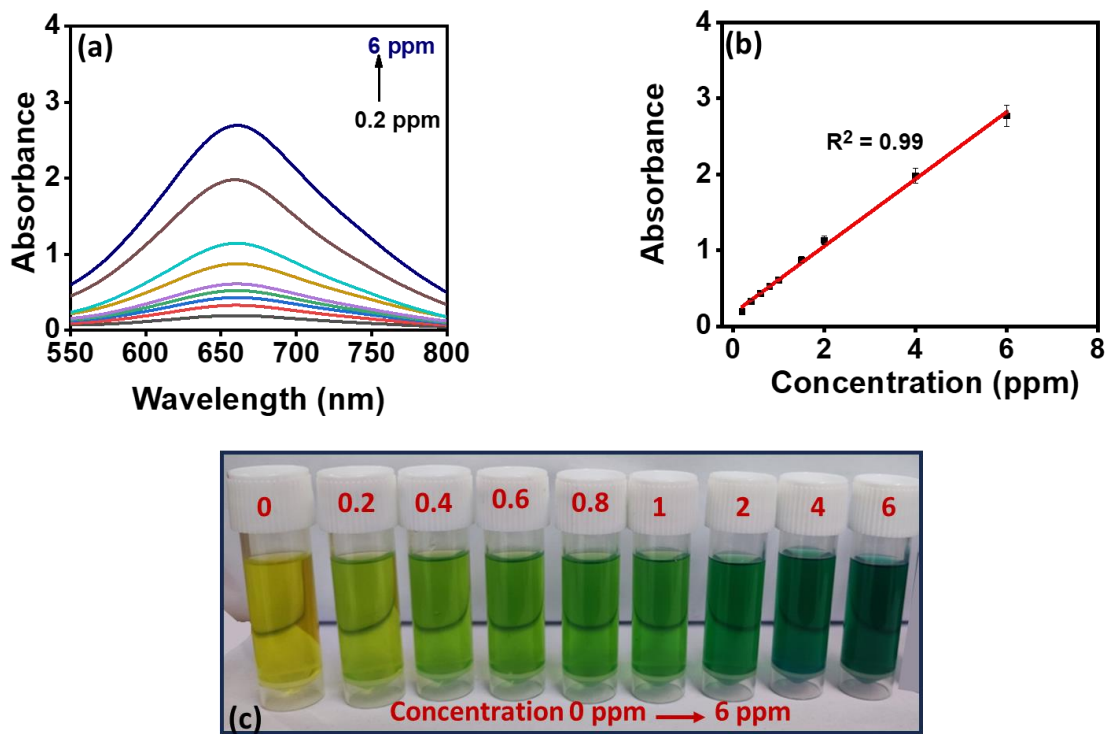
Fig. S6. (a) UV-Vis spectra and (b) corresponding calibration curves obtained from different concentrations of the standard solution of NH_3 *via* Indophenol blue method. (c) Photograph captured for different known concentrations of NH_3.
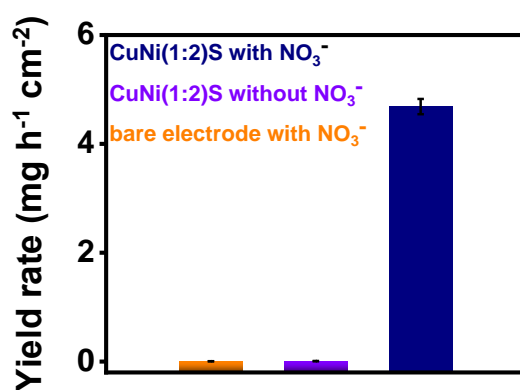
Fig. S7. NH_3 yield rate at bare Ni foam in the presence of NO_3^- and for CuNi(1:2)S catalyst in presence and absence of 100 mM KNO_3 in 1 M KOH.
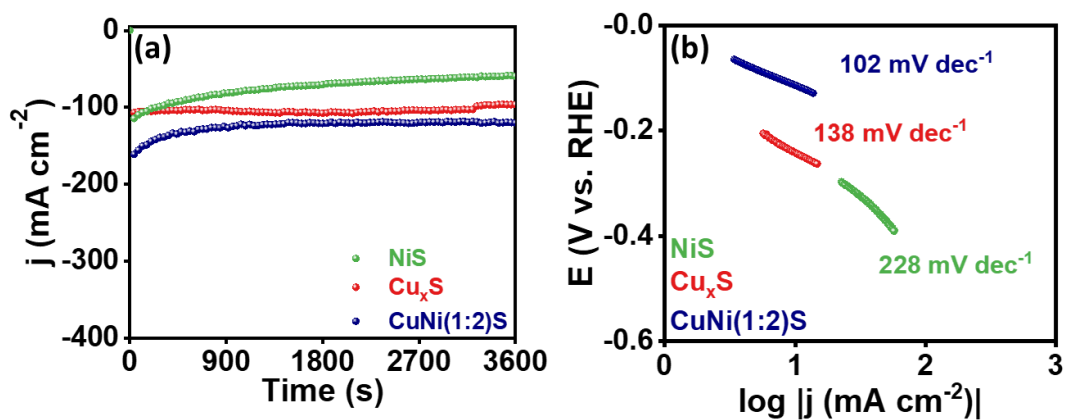
Fig. S8. Chronoamperometric curves at potentials of -0.4 V *vs.* RHE for (a) NiS, Cu_xS and CuNi(1:2)S catalyst and (b) Tafel slope extracted from LSV (Fig. 3a) of various catalysts in 100 mM KNO_3+1M KOH solution.
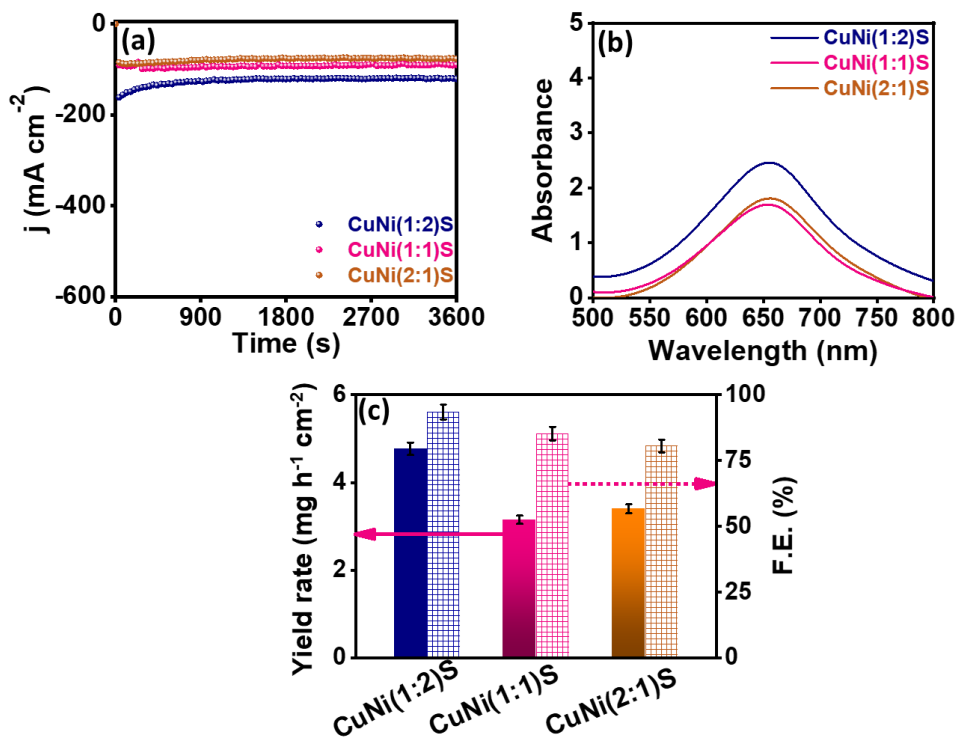
Fig. S9. (a) Chronoamperometric curve for CuNi(1:2)S, CuNi(1:1)S and CuNi(1:2)S catalyst in Ar saturated 100 mM KNO$_3$ + 1 M KOH solution at potential of -0.4 V *vs*. RHE (b) corresponding UV-Vis spectra of the electrolyte sample taken after chronoamperometry for NH$_3$ quantification *via* Indophenol blue method and (c) bar diagram representing corresponding NH$_3$ yield rate and F.E.
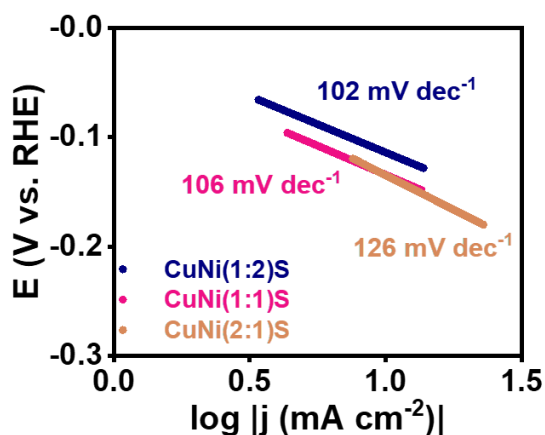

Fig. S10. Tafel slope extracted from LSV (Fig. S4) for CuNi(1:2)S, CuNi(1:1)S and CuNi(2:1)S catalyst in 100 mM KNO$_3$+1 M KOH solution.
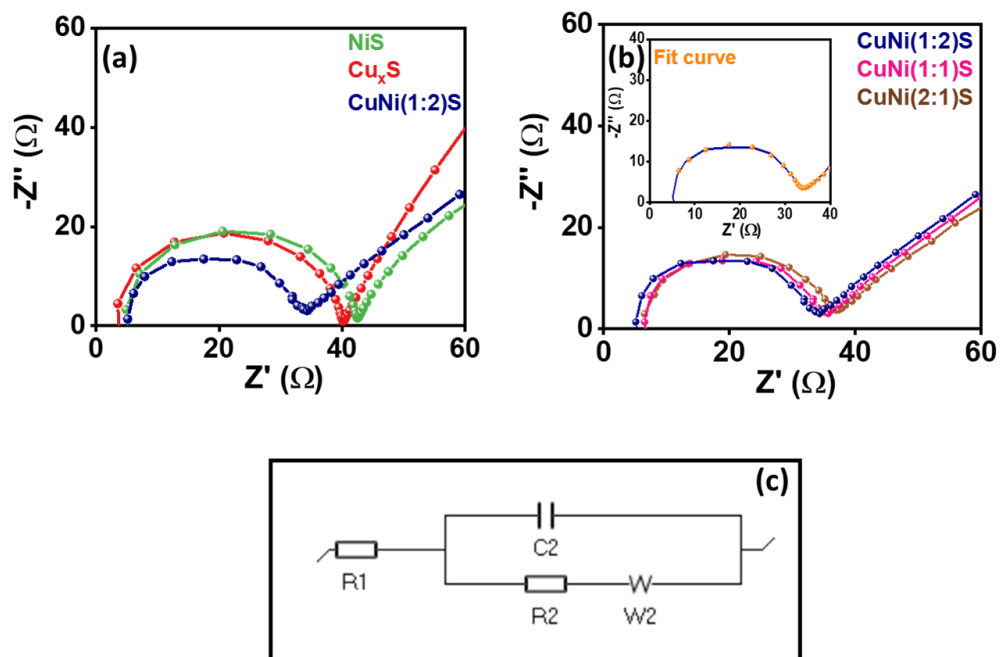
Fig. S11. Nyquist plots acquired in 100 mM KNO$_3$ in Ar saturated 1 M KOH for (a) CuNi(1:2)S, NiS and Cu$_x$S and (b) CuNi(1:2)S, CuNi(1:1)S and CuNi(2:1)S catalyst at a potential of -0.4 V *vs*. RHE in presence of NO$_3^-$ (inset showing fitted curve for CuNi(1:2)S) and (c) equivalent circuit for fitted Nyquist plot.
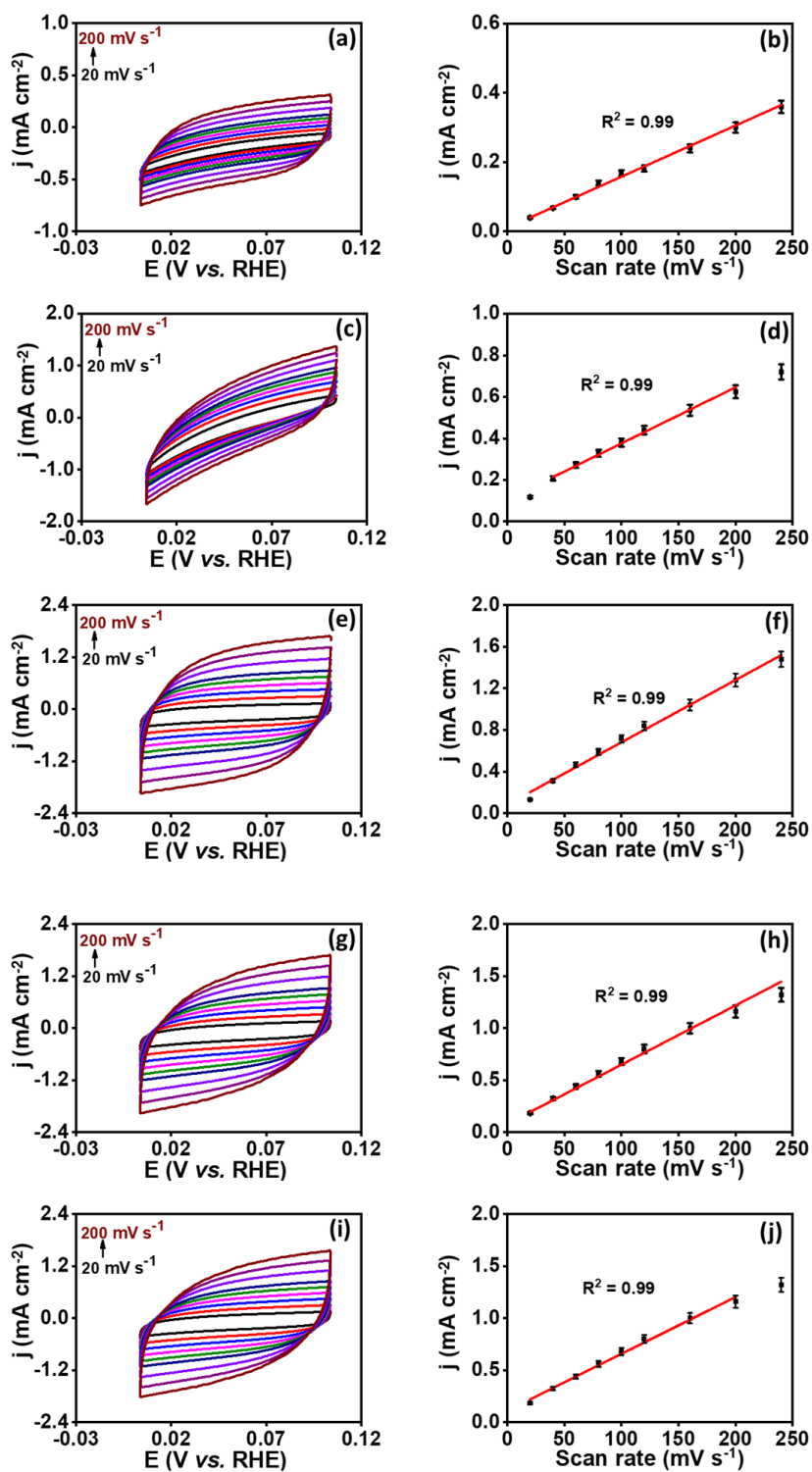
Fig. S12. (a, c, e, g, i) Cyclic voltammograms for NiS, Cu$_x$S, CuNi(1:2)S, CuNi(1:1)S and CuNi(2:1)S catalysts at various scan rates in Ar saturated 100 mM KNO$_3$+1 M KOH solution , and (b, d, f,h,j) current density *vs.* scan rate plots generated from the CVs.

Table S4. Tafel slope values extracted from LSV of catalysts in NO_3^- containing 1 M KOH.

Catalyst	Tafel slope (mV dec^{-1})
NiS	138
CuS	128
CuNi(1:2)S	102
CuNi(1:1)S	106
CuNi(2:1)S	126

Table S5. Electrochemical impedance analysis

Catalyst	R_S (Ω)	R_p (Ω)	R_{ct} (Ω)
NiS	5.11	42.64	37.53
Cu$_x$S	3.69	40.15	36.46
CuNi(1:2)S	5.26	34.0	28.74
CuNi(1:1)S	6.51	35.81	29.3
CuNi(2:1)S	6.51	37.05	30.54

Table S6. Electrochemical surface area (ECSA) measurements.

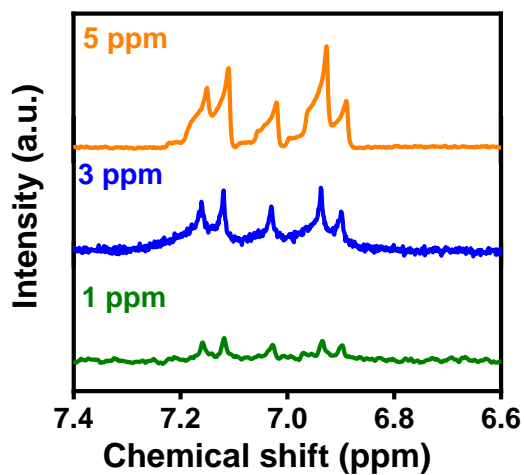| Catalyst	Cdl (µF) at 0.05 V	ECSA (cm^{-2})
NiS	369	9.25
CuS	675	16.87
CuNi(1:2)S	1500	37.5
CuNi(1:1)S	1420	35.5
CuNi(2:1)S	1370	34.25

Fig. S13A. ^{1}H-NMR spectra of an equimolar mixture of $^{14}NH_4Cl$ and $^{15}NH_4Cl$ solutions with varying concentrations ranging from 1 ppm to 5 ppm.
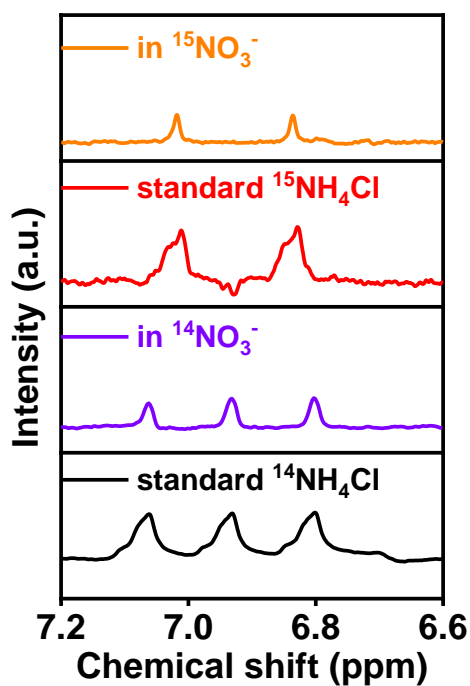
Fig. S13B ^{1}H NMR spectra of standard $^{15}NH_4Cl$ and $^{14}NH_4Cl$ samples and post-electrolytes using $^{15}NO_3^-$ and $^{14}NO_3^-$.
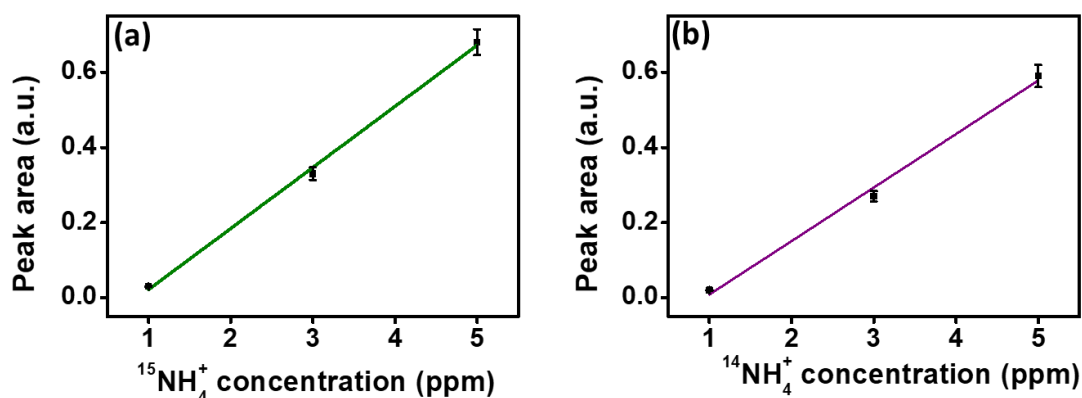
Fig. S14. Calibration curves for different standard concentration of NH_4^+ taken from ^1H NMR spectra for (a) $^{15}NH_4^+$ and (b) $^{14}NH_4^+$ respectively.
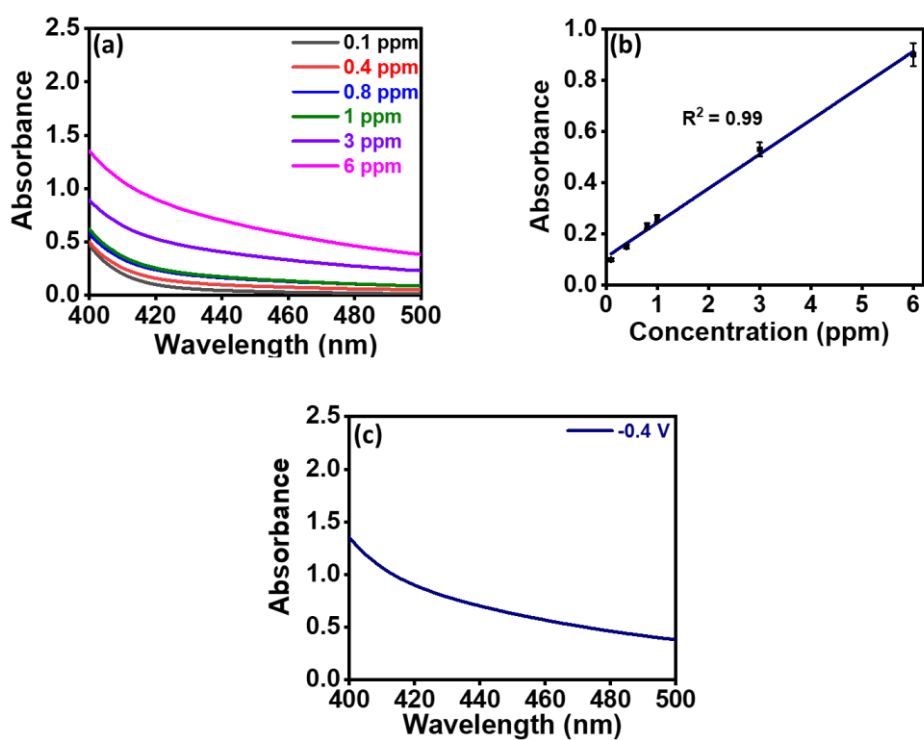

Fig. S15. (a) UV-Vis spectra for standard concentration of NH_3 after Nessler's reagent test and (b) its corresponding calibration curve. (c) UV-Vis spectra for NH_3 quantification using Nessler's reagent obtained after electrolysis of 1 h at potential of -0.4 V *vs*. RHE using CuNi(1:2)S catalyst.
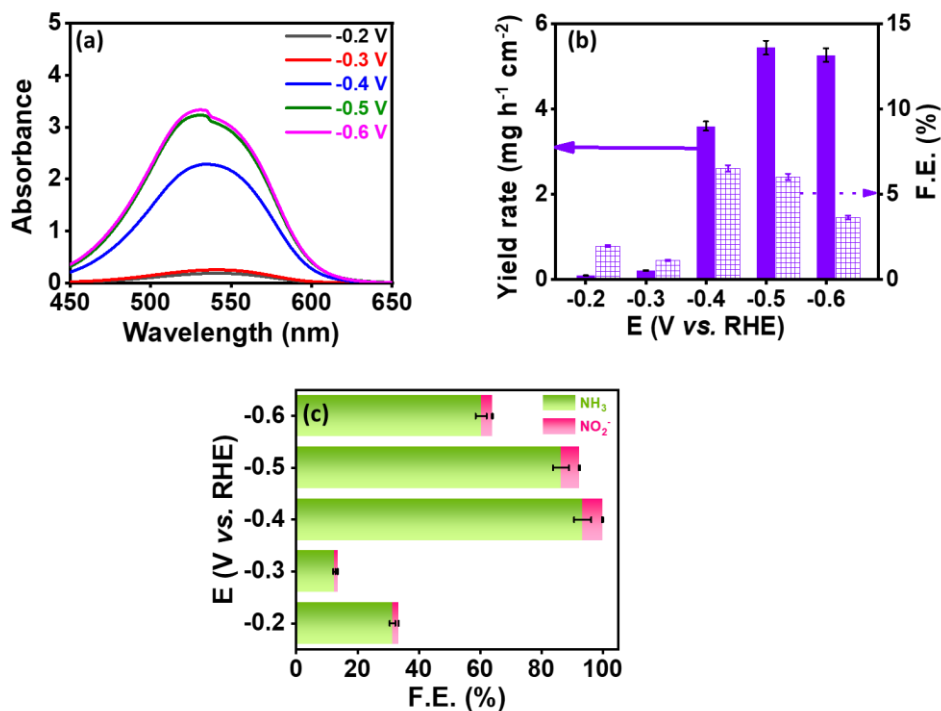
Fig. S16. (a) UV-Vis absorption spectra for nitrite (NO_2^-) obtained at different potential after chronoamperometry for 1 h and (b) its corresponding NO_2^- yield rate and F.E for CuNi(1:2)S catalyst. (c) Bar diagram representing F.E.s of different products (NH_3, NO_2^-) of CuNi(1:2)S obtained in 1 M KOH with 100 mM KNO_3 at different potentials.
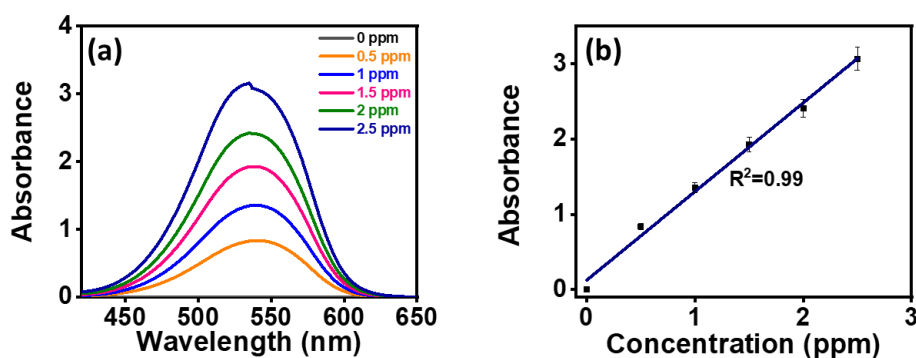

Fig. S17. (a) UV-Vis absorption spectra for various NO_2^- concentrations (b) corresponding calibration curve.
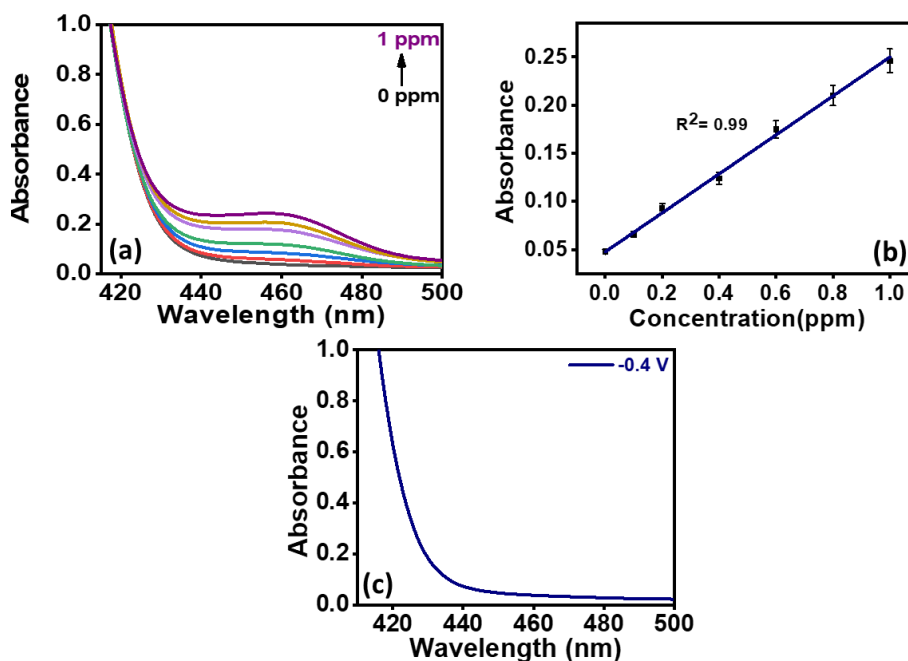
Fig. S18. (a) UV-Vis absorption spectra for standard hydrazine (N_2H_4) concentrations (b) corresponding calibration curve for detecting N_2H_4 concentration (c) UV-Vis absorption spectra for N_2H_4 after electrolysis at -0.4 V *vs.* RHE for CuNi(1:2)S catalyst.
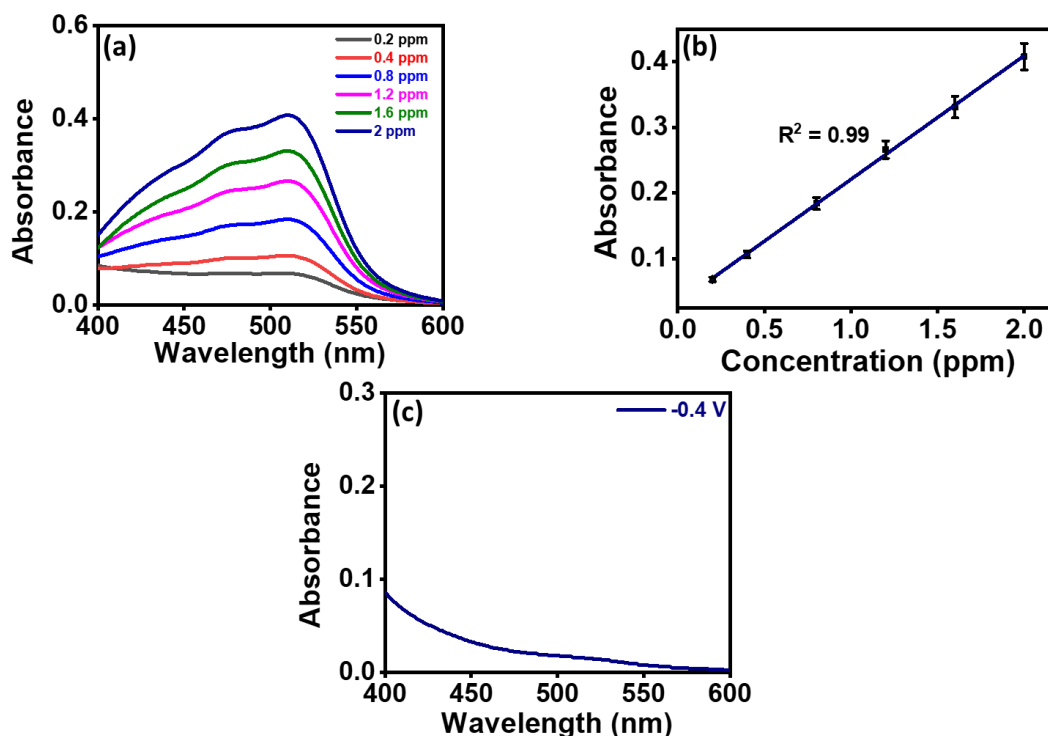

Fig. S19. (a) UV-Vis absorption spectra for standard hydroxylamine (NH_2OH) concentrations (b) corresponding calibration curve for detecting NH_2OH concentration (c) UV-Vis absorption spectra for NH_2OH after electrolysis at -0.4 V *vs*. RHE for CuNi(1:2)S catalyst.

Table S7. Comparison of NH_3 yield rates obtained after 1 h of NO_3RR by CuNi(1:2)S at -0.4 V *vs*. RHE for isotope labelling experiment by different methods.

Method of detection	$^{14}NH_3$ concentration (mg h^{-1} mg$^{-1}_{cat}$)	$^{15}NH_3$ concentration (mg h^{-1} mg$^{-1}_{cat}$)
Indophenol blue	4.76	4.73
^{1}H-NMR	4.83	4.70

Table S8. Comparison of NH_3 yield rate obtained after 1 h of NO_3RR by CuNi(1:2)S at -0.4 V *vs*. RHE.

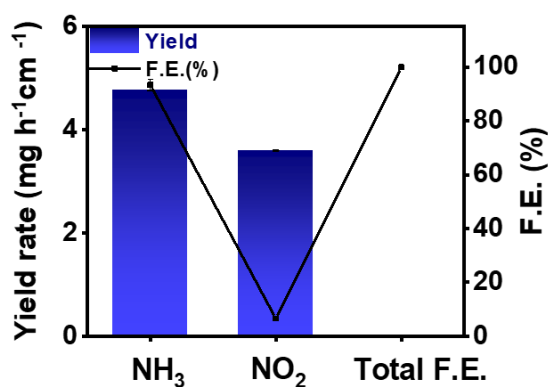| Method of detection	NH_3 yield rate (mg h^{-1} cm^{-2})
Indophenol blue	4.76
Nessler's reagent	4.72

Fig. S20. Bar diagram representing yield rate and F.E. of NH_3 and NO_2^- and total F.E. obtained after electrolysis at -0.4 V *vs*. RHE using CuNi(1:2)S catalyst.
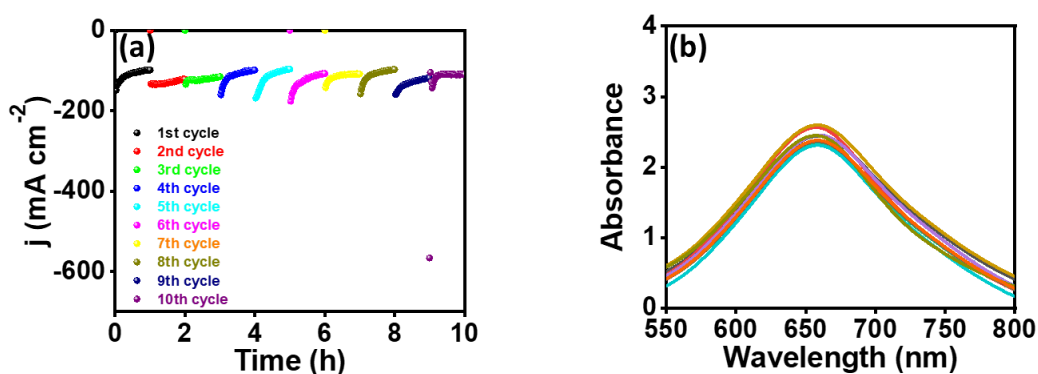
Fig. S21. (a) Chronoamperometric curve for consecutive 10 cycles at -0.4 V *vs*. RHE using CuNi(1:2)S catalyst and (b) corresponding UV-Vis absorption spectra.
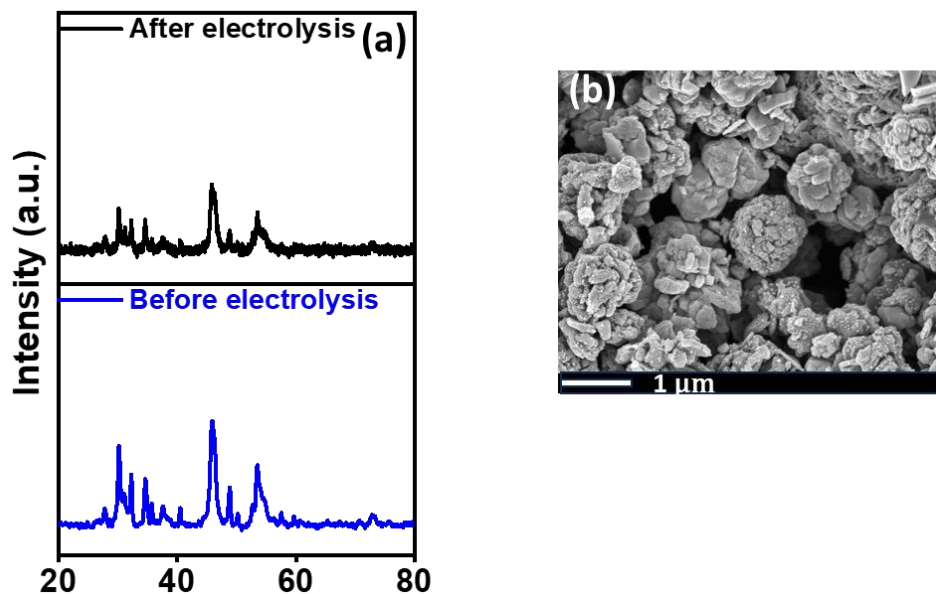
Fig. S22. (a) XRD analysis before and after stability test (b) Post FE-SEM image for CuNi(1:2)S catalyst after NO_3RR stability test.
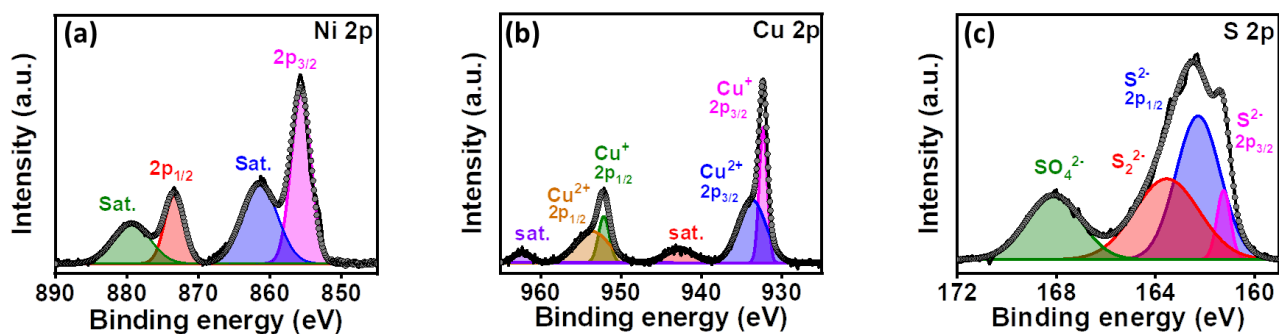

Fig. S23. Deconvoluted XP spectra of (a) Ni 2p, (b) Cu 2p, (c) S 2p, for CuNi(1:2)S catalyst after NO_3RR stability test.

Table S9: Comparison of NO₃RR, OER, and GOR activity activity for different catalyst.

Catalyst	Electrolyte	NH₃ F.E.(%)	NH₃ yield rate	OER (V vs. RHE)	GOR (V vs. RHE)	Reference
CuNi(1:2)S	**1 M KOH + 100 mM KNO₃**	**93.44% @ -0.4 V vs. RHE**	**8.05 mg h⁻¹ cm⁻² or 473.47 mmol g_{cat}⁻¹ h⁻¹ @ -0.6 V vs. RHE**	**1.55**	**1.35**	**Our work**
Ru-Tta-Dfp	1 M KOH + 100 mM KNO₃	93.93 %	1.16 mg h⁻¹ cm⁻² @ -0.4 V vs. RHE	1.62	1.27	[14]
Iridium nanotubes	0.1 M HClO₄ + 1 M NaNO₃	~84.7 %	921 µg h⁻¹ mg_{cat}⁻¹	1.477	-	[15]
CuPd nanocubes	1 M KOH + 1 M KNO₃	92.5% @ -0.5 V	6.25 mol g⁻¹_{cat} h⁻¹ @ -0.6 V	-	-	[16]
Fe single atom/C	0.1 M K₂SO₄ + 0.5 M KNO₃	75% @ -0.66 V	0.46 mmol h⁻¹ cm⁻² @ -0.66 V	-	-	[17]
Cu/Cu₂O	0.5 M Na₂SO₄ +200 ppm NO₃⁻-N	95.8% @ -0.85 V	0.245 mmol h⁻¹ cm⁻² @ -0.85 V	-	-	[18]
Cu@Th-BPYDC	1 M KOH + 100 mM KNO₃	92.5% @ 0 V	3.83 mg cm⁻² h⁻¹@ 0 V	-	-	[19]
Cu@Cu₂₊₁O NWs	0.5 M K₂SO₄ + 50 mg L⁻¹ NO₃⁻-N	87.07% @ -1.2 V vs. SCE	0.57 mg cm⁻² h⁻¹@ -1.2 V vs. SCE	-	-	[20]
Fe₃O₄@TiO₂/TP	0.1 M phosphate-buffer + 0.1 M NaNO₃	88.4% @ -0.9 V	12.39 mg h⁻¹ cm⁻²@ -0.9 V vs. RHE	-	-	[21]
CuFe/OMC	0.1 M PBS + 500 ppm NO₃⁻	~78%	2.37 mg h⁻¹ cm⁻² @ -0.4 V vs. RHE	-	-	[22]
Fe₃O₄/stainless steel	0.1 M NaOH + 0.1 M NaNO₃	91.5% @ -0.5 V vs. RHE	10.15 mg h⁻¹ cm⁻²@ -0.5 V vs. RHE	-	-	[23]
Rh@Cu	0.1 M Na₂SO + 100 mM KNO₃	93.0% @ -0.2 V vs. RHE	1.27 mmol h⁻¹ cm⁻²@ -0.2 V vs. RHE	-	-	[24]
Co-Fe/Fe₂O₃	0.1 M Na₂SO₄ + 50 ppm NO₃⁻-N	85.2% @ -0.75 V vs. RHE	1.51 mg h⁻¹ cm⁻² @ -0.75 V vs. RHE	-	-	[25]

|						
CuCoSP	0.1 M KOH + 0.01 M KNO$_3$	~93.3% ± 2.1% @ −0.175 V vs. RHE	1.170 mmol h^{-1} cm^{-2}	-	-	4
Cu-Fe$_2$O$_3$	0.5 M Na$_2$SO$_4$ + 50 ppm NO$_3^-$-N	80.1% @ -0.6 V vs. RHE	0.108 mmol h^{-1} cm^{-2} @ -0.6 V vs. RHE	-	-	26
Cu−N−CSAC	0.1 M KOH + 0.1 M KNO$_3$	84.7% @−1.0 V vs. RHE	0.26 mmol h^{-1} cm^{-2} @−1.0 V vs. RHE	-	-	27
Cu nanodisks	0.1 M KOH + 10 mM KNO$_3$	81.1 % @ -0.5 V *vs.* RHE	2.16 mg h^{-1} mg^{-1} cat @ -0.5 V *vs.* RHE	-	-	28
Cu-Ni tandem	1 M KOH +100 mM KNO$_3$	88 % @ -1 V	0.58 mmol h^{-1} cm^{-2} @ -1 V	-	-	29
CuNi/NC	0.1 M PBS+ 50 ppm NO$_3^-$-N	79.6 %	-	-	-	30
CuNi NPs/CF	1 M NaOH + 44.3 g L^{-1} NO$_3^-$	97.03 %	94.57 mg h^{-1} cm^{-2} @ -0.48 V *vs.* RHE	-	-	31
Cu$_{0.25}$Ni$_{0.25}$	1 M KOH + 75 mM KNO$_3$	94.5 %	9.34 mg h^{-1} cm^{-2}@ -0.3 V *vs.* RHE	-	-	1
CuNi-NC	0.5 M Na$_2$SO$_4$ +100 ppm NaNO$_3$	97.3 %	5.48 mg h^{-1} cm^{-2}@ -0.7 V *vs.* RHE	-	-	32
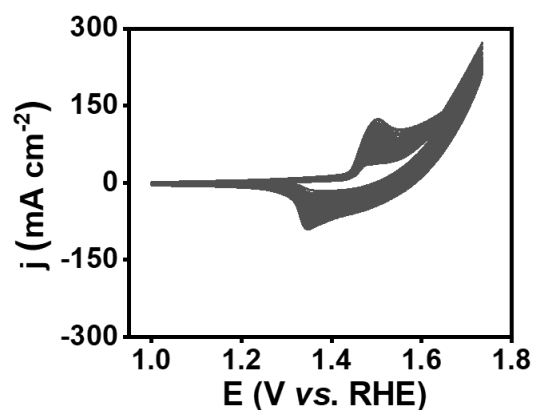
Fig. S24. CV for CuNi(1:2)S catalyst for 50 cycle in 1 M KOH solution at scan rate of 50 mV s^{-1}.
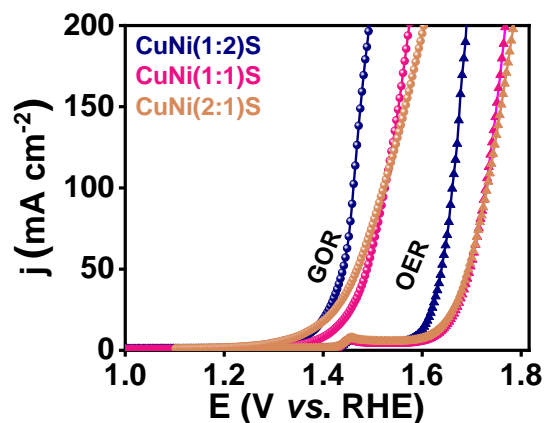
Fig. S25.LSV curves for CuNi(1:1)S, CuNi(2:1)S and CuNi(1:2)S catalyst at a scan rate of 5 mV s^{-1} in the presence (GOR) and absence (OER) of glucose in 1M KOH solution
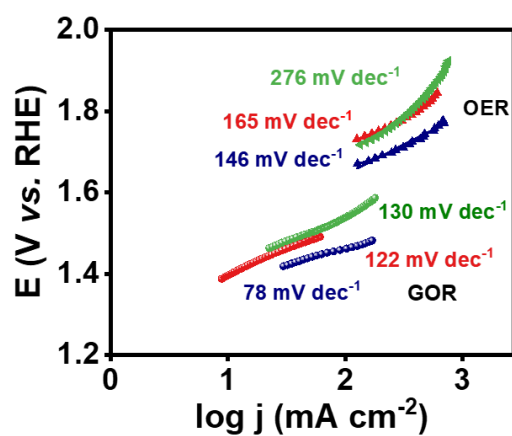

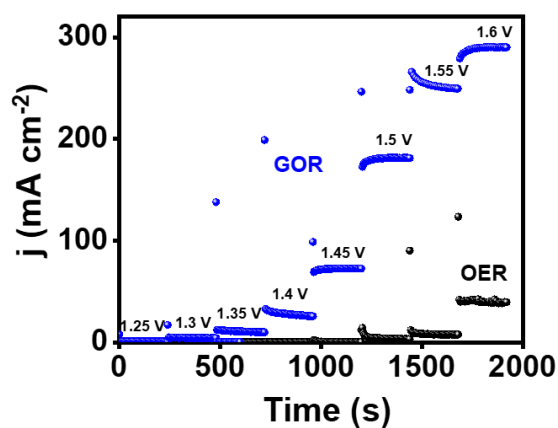**Fig. S26.**Tafel slope extracted from LSV (Fig. 5a) for catalyst in presence and absence of glucose.

Fig. S27. Sequential chronoamperometry at different potentials for CuNi(1:2)S at an interval of 0.05 V for GOR and OER activity.
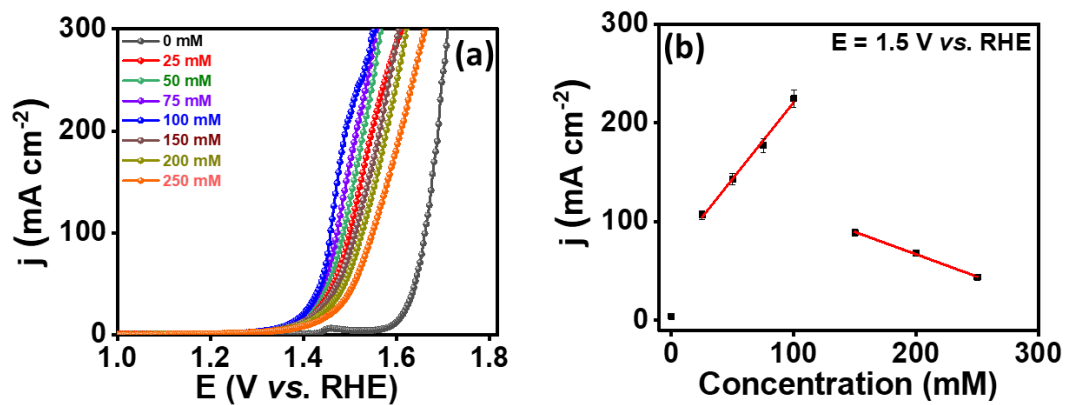
Fig. S28. LSV for different concentration of glucose with its corresponding linear plot.
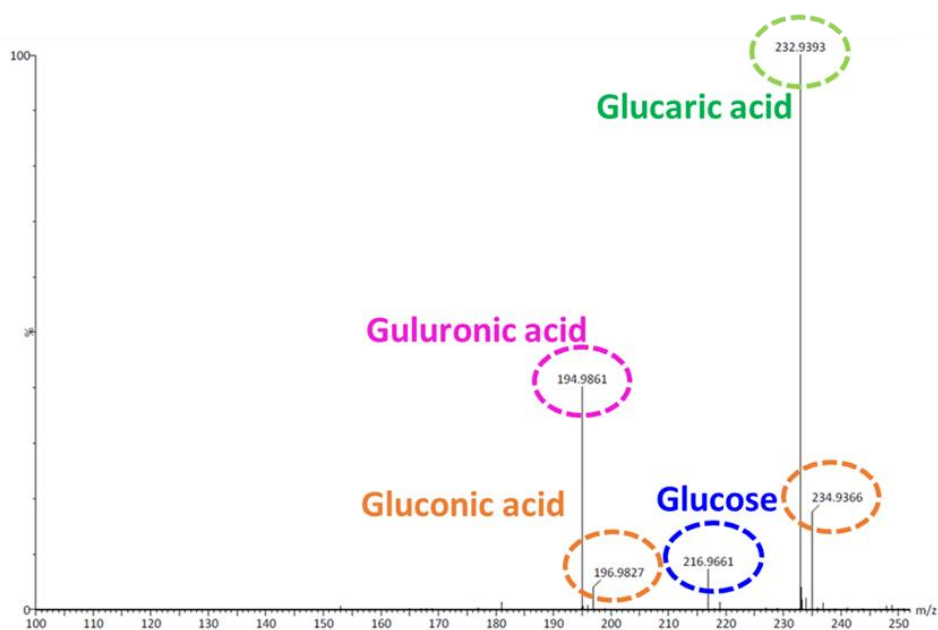
Fig. S29. HRMS spectra of electrolyte after glucose oxidation.

Table S10: High Resolution Mass Spectra (HRMS) analysis

Compounds	Molecular mass	Adducts
Glucose	180	216.96 (M+2H$_2$O)
Guluronic acid	194.98	194.98 (M)
Gluconic acid	196.16	196.98 (M+H)
		234.93 (M+ K$^+$)
Glucaric acid	210	232.93 (M+K$^+$-H$_2$O+H)

Fig. S30. Chronoamperometric curves after electrolysis different current density of 50 and 100 mA cm^{-2} for 15 h for GOR using CuNi(1:2)S catalyst.

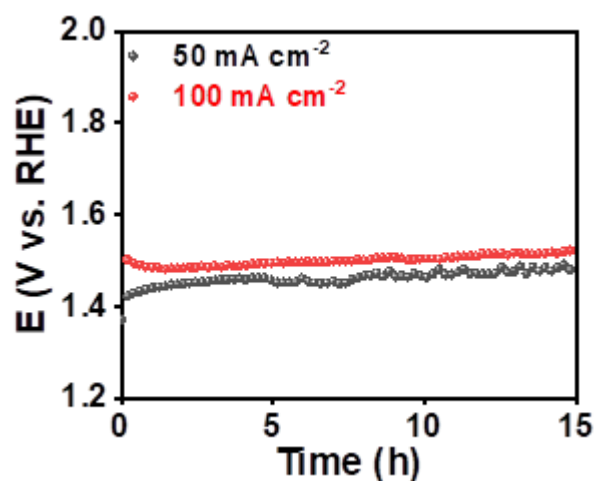**Table S11. Comparison of CuNi(1:2)S catalyst with others previously reported catalyst for electrochemical glucose oxidation.**

| Catalyst	Voltage (V)	Current density (mA cm^{-2})	Product	Ref.
CuNi(1:2)S	**1.44**	**50**	**Glucose, guluronic acid, gluconic acid, glucaric acid**	**Our Work**
Fe$_2$P/SSM	1.22	10	-	[33]
	1.51	50		
	1.58	100		
NiFeOx-NF	1.33	50	Gluconic acid, glucaric acid,	[34]
	1.39	100		
Cu(OH)$_2$	0.74	10	Gluconic acid	[35]
	0.83	50		
	0.92	100		
CF@CoNC-2T	0.90	100	Gluconic acid, guluronic acid, glucaric acid	[36]
Ni–MoS$_2$ NPs	1.67	10	-	[37]
NiV(2:1)P/Pi-VC	1.3	10	Gluconolactone, gluconic acid, Glucaric acid	[38]
Fe$_{0.1}$-CoSe$_2$/CC	0.72	10	Gluconate	[39]
CNT@Co/CoP	1.42	10	Gluconate, gluconic acid	[40]
Co@NPC	1.56	10	Lactic acid, Formic acid	[41]
CoWO$_4$(12 h)	1.44	10	Gluconolactone, gluconic acid, glucaric acid, guluronic acid	[42]
Ru-Tta-Dfp COF	1.27	10	Glucose, guluronic acid gluconic acid, glucaric acid,	[14]
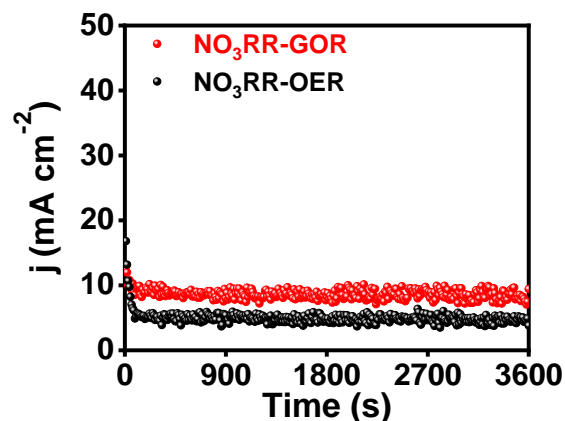
Fig. S31. Chronoamperometric curves after electrolysis at 1.5 V for NO₃RR-OER and NO₃RR-GOR using CuNi(1:2)S catalyst.

References

1. X. Wang, X. Chi, Z. Fu, Y. Xiong, S. Li, Y. Yao, K. Zhang, Y. Li, S. Wang, R. Zhao, Z. Yang and Y.-M. Yan, *Appl. Catal. B*, 2023, **322**, 122130.
2. H.-J. Shin, W. M. Choi, D. Choi, G. H. Han, S.-M. Yoon, H.-K. Park, S.-W. Kim, Y. W. Jin, S. Y. Lee, J. M. Kim, J.-Y. Choi and Y. H. Lee, *J. Am. Chem. Soc.*, 2010, **132**, 15603-15609.
3. P. H. van Langevelde, I. Katsounaros and M. T. Koper, *oule*, 2021, **5**, 290-294.
4. W. He, J. Zhang, S. Dieckhöfer, S. Varhade, A. C. Brix, A. Lielpetere, S. Seisel, J. R. C. Junqueira and W. Schuhmann, *Nat. Commun.*, 2022, **13**, 1129.
5. E. Pérez-Gallent, M. C. Figueiredo, I. Katsounaros and M. T. M. Koper, *Electrochim. Acta*, 2017, **227**, 77-84.
6. Y. Zhao, R. Shi, X. Bian, C. Zhou, Y. Zhao, S. Zhang, F. Wu, G. I. N. Waterhouse, L.-Z. Wu, C.-H. Tung and T. Zhang, *Adv. Sci.*, 2019, **6**, 1802109.
7. G. W. Watt and J. D. J. A. C. Chrisp, *J. Anal. Chem.*, 1952, **24**, 2006-2008.
8. L. Li, C. Tang, D. Yao, Y. Zheng and S.-Z. Qiao, *ACS Energy Lett.*, 2019, **4**, 2111-2116.
9. L. C. Green, D. A. Wagner, J. Glogowski, P. L. Skipper, J. S. Wishnok and S. R. Tannenbaum, *Anal. Biochem.*, 1982, **126**, 131-138.
10. Y. Shi, S. Xu and F. Li, *Chem. Commun.*, 2022, **58**, 8714-8717.
11. R. Zhang, Y. Guo, S. Zhang, D. Chen, Y. Zhao, Z. Huang, L. Ma, P. Li, Q. Yang and G. Liang, *Adv. Energy Mater.*, 2022, **12**, 2103872.
12. Y. Wang, A. Xu, Z. Wang, L. Huang, J. Li, F. Li, J. Wicks, M. Luo, D.-H. Nam, C.-S. Tan, Y. Ding, J. Wu, Y. Lum, C.-T. Dinh, D. Sinton, G. Zheng and E. H. Sargent, *J. Am. Chem. Soc.*, 2020, **142**, 5702-5708.
13. H. Liu, X. Lang, C. Zhu, J. Timoshenko, M. Rüscher, L. Bai, N. Guijarro, H. Yin, Y. Peng, J. Li, Z. Liu, W. Wang, B. R. Cuenya and J. Luo, *Angew. Chem. Int. Ed.*, 2022, **61**, e202202556.
14. A. Chaturvedi, S. Gaber, S. Kaur, K. C. Ranjeesh, T. C. Nagaiah and D. Shetty, *ACS Energy Lett.*, 2024, **9**, 2484-2491.
15. J.-Y. Zhu, Q. Xue, Y.-Y. Xue, Y. Ding, F.-M. Li, P. Jin, P. Chen and Y. Chen, *ACS Appl. Mater. Interfaces*, 2020, **12**, 14064-14070.
16. Q. Gao, H. S. Pillai, Y. Huang, S. Liu, Q. Mu, X. Han, Z. Yan, H. Zhou, Q. He, H. Xin and H. Zhu, *Nat. Commun.*, 2022, **13**, 2338.

17.	Z.-Y. Wu, M. Karamad, X. Yong, Q. Huang, D. A. Cullen, P. Zhu, C. Xia, Q. Xiao, M. Shakouri, F.-Y. Chen, J. Y. Kim, Y. Xia, K. Heck, Y. Hu, M. S. Wong, Q. Li, I. Gates, S. Siahrostami and H. Wang, *Nat. Commun.*, 2021, **12**, 2870.
18.	Y. Wang, W. Zhou, R. Jia, Y. Yu and B. Zhang, *Angew. Chem.*, 2020, **59**, 5350-5354.
19.	Z. Gao, Y. Lai, Y. Tao, L. Xiao, L. Zhang and F. Luo, *ACS Cent. Sci.*, 2021, **7**, 1066-1072.
20.	T. Ren, K. Ren, M. Wang, M. Liu, Z. Wang, H. Wang, X. Li, L. Wang and Y. Xu, *Chem. Eng. J.*, 2021, **426**, 130759.
21.	X. He, J. Li, R. Li, D. Zhao, L. Zhang, X. Ji, X. Fan, J. Chen, Y. Wang, Y. Luo, D. Zheng, L. Xie, S. Sun, Z. Cai, Q. Liu, K. Ma and X. Sun, *Inorg. Chem.*, 2023, **62**, 25-29.
22.	J. Zhao, L. Liu, Y. Yang, D. Liu, X. Peng, S. Liang, L. Jiang and Engineering, *ACS Sustain. Chem. Eng.*, 2023, **11**, 2468-2475.
23.	X. Fan, L. Xie, J. Liang, Y. Ren, L. Zhang, L. Yue, T. Li, Y. Luo, N. Li, B. Tang, Y. Liu, S. Gao, A. A. Alshehri, Q. Liu, Q. Kong and X. Sun, *Nano Res.*, 2022, **15**, 3050-3055.
24.	H. Liu, X. Lang, C. Zhu, J. Timoshenko, M. Rüscher, L. Bai, N. Guijarro, H. Yin, Y. Peng, J. Li, Z. Liu, W. Wang, B. R. Cuenya and J. Luo, *Angew. Chem. Int. Ed.*, 2022, **61**, e202202556.
25.	S. Zhang, M. Li, J. Li, Q. Song and X. Liu, *Proc Natl Acad Sci U S A*, 2022, **119**.
26.	Y. Gao, K. Huang, C. Yan, S. Li, H. Zhang, L. Cheng and F. Huang, *Mater. Adv.*, 2022, **3**, 7107-7115.
27.	J. Yang, H. Qi, A. Li, X. Liu, X. Yang, S. Zhang, Q. Zhao, Q. Jiang, Y. Su, L. Zhang, J.-F. Li, Z.-Q. Tian, W. Liu, A. Wang and T. Zhang, *J. Am. Chem. Soc.*, 2022, **144**, 12062-12071.
28.	K. Wu, C. Sun, Z. Wang, Q. Song, X. Bai, X. Yu, Q. Li, Z. Wang, H. Zhang, J. Zhang, X. Tong, Y. Liang, A. Khosla and Z. Zhao, *ACS mater. lett.*, 2022, **4**, 650-656.
29.	Y. Bu, C. Wang, W. Zhang, X. Yang, J. Ding and G. Gao, *Angew. Chem.*, 2023, **62**, e202217337.
30.	Y. Liu, B. Deng, K. Li, H. Wang, Y. Sun and F. Dong, *J. Colloid Interface Sci.*, 2022, **614**, 405-414.
31.	W. Yu, J. Yu, M. Huang, Y. Wang, Y. Wang, J. Li, H. Liu and W. Zhou, *Energy Environ. Sci.*, 2023, **16**, 2991-3001.
32.	Y. Wang, H. Yin, F. Dong, X. Zhao, Y. Qu, L. Wang, Y. Peng, D. Wang, W. Fang and J. Li, *Small*, 2023, **19**, 2207695.
33.	P. Du, J. Zhang, Y. Liu and M. Huang, *Electrochem. Commun.*, 2017, **83**, 11-15.
34.	W.-J. Liu, Z. Xu, D. Zhao, X.-Q. Pan, H.-C. Li, X. Hu, Z.-Y. Fan, W.-K. Wang, G.-H. Zhao, S. Jin, G. W. Huber and H.-Q. Yu, *Nat. Commun.*, 2020, **11**, 265.
35.	Y. Zhang, B. Zhou, Z. Wei, W. Zhou, D. Wang, J. Tian, T. Wang, S. Zhao, J. Liu, L. Tao and S. Wang, *Adv. Mater.*, 2021, **33**, 2104791.
36.	Y. Xin, F. Wang, L. Chen, Y. Li and K. Shen, *Green Chemistry*, 2022, **24**, 6544-6555.
37.	X. Liu, P. Cai, G. Wang and Z. Wen, *Int. J. Hydrogen Energy*, 2020, **45**, 32940-32948.
38.	N. Thakur, D. Mehta, A. Chaturvedi, D. Mandal and T. C. Nagaiah, *J. Mater. Chem. A*, 2023, **11**, 15868-15877.
39.	D. Zheng, J. Li, S. Ci, P. Cai, Y. Ding, M. Zhang and Z. Wen, *Appl. Catal. B*, 2020, **277**, 119178.
40.	Y. Zhang, Y. Qiu, Z. Ma, Y. Wang, Y. Zhang, Y. Ying, Y. Jiang, Y. Zhu and S. Liu, *J. Mater. Chem. A*, 2021, **9**, 10893-10908.
41.	D. Li, Y. Huang, Z. Li, L. Zhong, C. Liu and X. Peng, *Chem. Eng. J.*, 2022, **430**, 132783.
42.	A. Chaturvedi, D. Gupta, S. Kaur, K. Garg and T. C. Nagaiah, *J. Mater. Chem. A*, 2023, **11**, 18280-18290.